Morphing of a supercritical wing by means of trailing edge deformation and vibration at high Reynolds numbers: Experimental and numerical investigation

Nikolaos Simiriotis, Gurvan Jodin, Abderahmane Marouf, P. Elyakime, Yannick Hoarau, J.C.R. Hunt, Jean-François Rouchon, Marianna Braza

Morphing of a supercritical wing by means of trailing edge deformation and vibration at high Reynolds numbers: experimental and numerical investigation

N. Simiriotis[a,*], G. Jodin[a,b], A. Marouf[a,c], P. Elyakime[a], Y. Hoarau[c], J.C. Hunt[d], J.F. Rouchon[b], M. Braza[a]

[a] *Institut de Mcanique des Fluides de Toulouse (IMFT), UMR 5502 CNRS-INPT-UPS, 2 Alle du Professeur Camille Soula, 31400 Toulouse, France*
[b] *Laboratoire Plasma et Conversion d'Energie (LAPLACE), UMR 5213 CNRS-INPT, 2 rue Charles Camichel, 31071 Toulouse, France*
[c] *Laboratoire iCUBE, UMR7357 CNRS-Universit de Strasbourg, 300 Bd Sbastien Brant, 67400 Illkirch-Graffenstaden, France*
[d] *University College London, Gower Street, London WC1E 6BT, England*

Abstract

This article examines the morphing effects of the trailing-edge deformation and vibration on the turbulent structures in the wake of a supercritical Airbus-320 wing. It is shown that the electroactive morphing has the capacity to produce an enhanced aerodynamic performance (lift increase, drag reduction) and reduce the amplitude of instability modes associated to aerodynamic noise. The appropriate actuation is achieved with piezoactuators placed in the trailing edge region. The work presented has been carried out numerically using the Navier-Stokes Multi Block (NSMB) code, as well as experimentally with measurements obtained in the S4 wind tunnel of IMFT by means of TRPIV (Time-Resolved PIV) with a sampling rate around 10 KHz. The Reynolds number is 1 Million. The study is carried out in the low subsonic regime at an incidence angle of 10°, corresponding to take-off/landing flight phases and analyses significant morphing effects obtained by optimal deformations and vibrations of the near trailing edge region. The interactions that are prompted in the wake region are analyzed by

*Corresponding author
Email addresses: nikolaos.simiriotis@imft.fr (N. Simiriotis), jodin@laplace.univ-tlse.fr (G. Jodin), marouf.abderahmane@imft.fr (A. Marouf), Pierre.Elyakime@imft.fr (P. Elyakime), hoarau@unistra.fr (Y. Hoarau), julian.hunt@ucl.ac.uk (J.C. Hunt), rouchon@laplace.univ-tlse.fr (J.F. Rouchon), marianna.braza@imft.fr (M. Braza)

means of Proper Orthogonal Decomposition (POD), considering the near wake structure in respect of the morphing effects. The effects on the aerodynamic coefficients thanks to manipulation of specific vortex dynamics in the shear layers and the wake are discussed and optimal frequency/amplitude ranges for the vibrations are quantified.
Keywords: bio-inspiration, electroactive morphing, turbulence, control, flow dynamics, interfaces

---

1. Introduction

This study aims at highlighting the capacity of morphing to increase lift, decrease drag and reduce the amplitude of instability modes associated to aerodynamic noise. An exact definition of morphing is not agreed between researchers regarding the type or the extent of the geometrical changes necessary [1]. In [2] the word *morphing* is defined as an efficient multi-point adaptability. In this paper, morphing refers to the adaptation in real-time of the shape and vibrational behavior of the aerodynamic surface. A multi-disciplinary research platform involving the IMFT (Institut de Mécanique des Fluides de Toulouse) and LAPLACE (Laboratoire Plasma et Conversion d'Energie) has been continuously working in this topic since 2010, originally thanks to the support of the Foundation STAE (http://www.fondation-stae.net/). By this synergistic platform among six Institutes in Toulouse (www.smartwing.org) coordinated by IMFT and in close collaboration with AIRBUS *Emerging Technologies and Concepts Toulouse*, advanced *electroactive* morphing designs for the wings of the future were born. This answers to the demand for innovative morphing designs heading towards a highly efficient *green* aircraft [1] bringing possible structural solutions [3]. Currently, electroactive morphing is being studied and developed in the context of the European research program of H2020, "Smart Morphing & Sensing for Aeronautical configurations" (www.smartwing.org/SMS/EU). In particular, the *hybrid* morphing concept, partly bio-inspired, was introduced ([4], [5]) to operate at various time scales.

This concept utilizes different classes of electroactive actuators: Shape Memory Alloys able to achieve high deformations at low frequencies (order of 1Hz) imitating the camber effect of large-span hunting birds, as well as piezoactuators producing higher

frequency vibrations (order of hundreds of Hz) at low deformations. These last correspond to the action of bird feathers which by vibrating at higher frequencies are able to produce significant vortex breakdown, beneficial for the aerodynamic performance. When these actuations are realized simultaneously in the context of hybrid morphing, modification of turbulence can be achieved at multiple scales. It enables the manipulation of the turbulence and its interaction with the morphing structure, enhancing the amplification of smaller vortex structures in the wake and attenuating harmful ones. This bio-inspired morphing allows a smart wing design through turbulence control - science imitating nature, as mentioned in the annual exhibition of our morphing prototypes at the Royal Society, `http://sse.royalsociety.org/2014/smart-wing-design/`.

Bio-inspired technologies and designs have been considered in various morphing applications. In [6] and [7], biologically inspired compliant structures have been developed to provide continuous camber changes and were tested displaying enhanced aerodynamic efficiency. Compliant structures are needed in order to maintain the actuation forces in low levels. This is a key challenge for morphing structures [3] as they should be at the same time able to be carrying significant prescribed loading. However, the potential gain in the capabilities of future vehicles is broad and recent developments in *smart* materials - such are materials used in the present prototype - aid to overcome the limitations and provide a change in shape with no distinction between the structure and the actuation system [1].

This study focuses in high Reynolds number (order of 10^6). Previous studies in the literature were carried out at low Reynolds numbers [8], [9] examined part of the flow characteristics and although useful in the analysis, are quite limited and not operating in multiple scales. Past papers have also examined the forcing of the trailing of a wing [10] also in lower Reynolds number. The flow in the supercritical Reynolds range presents complex vortex dynamics and interactions with the solid structure, calling for specific attention in order to produce successful morphing effects. High Reynolds dynamics change the general flow behaviour and the morphing practices and targets. In the present context, the electro-active morphing is a more general strategy than standard flow control techniques as it creates fluid-structure interactions and inter-optimality among structural dynamics and turbulence manipulation.

In the present article, the electroactive morphing effects around an Airbus-A320 wing are presented at a Reynolds number of 1 million and an angle of incidence of 10°, by means of numerical simulation and experimental investigation. Both the Reynolds range and the angle of attack corresponding to take-off/landing flight phases. A previous experimental study in [5] has presented a first analysis of the morphing effects. The present article enlightens the morphing effects regarding the aerodynamic performance, by a synergy between numerical simulation and experiments, which is an original element in the state of the art.

1.1. Prototype design

The considered prototype is a design of an electroactive hybrid morphing wing. It is equipped with both a camber control system and High Frequency Vibrating Trailing Edge (HFVTE) actuators. The baseline airfoil is the wing section of Airbus-A320, with a chord of $700mm$ and a span of $590mm$. The camber control actuators were sized and implemented on a length covering the last 30% of the chord, corresponding to the actual flap placement. The area at the leading edge was retained hollow to provide the space to contain all electronics and tubing necessary for temperature, pressure and position transducers as well as actuator interfaces.

The working principle of the camber control relies on distributed structure embedded actuators. Shape Memory Alloy (SMA) wires are placed under the upper and lower sides of the aluminum sheets constituting the skin of the wing. The selected SMA wires were made of Nickel-Titanium alloys and their properties are controlled by a change in temperature [11]. When electrically charged, the wires are heated and are able to recover part of the strain by which they have been previously trained. They are capable of generating intense stress (larger than $600MPa$) under these large deformation levels and can be respectively cooled down by forced air to return to the initial pre-trained position. The SMA wires are capable of providing high deformations of order $25-30\%$ of the chord at low frequencies (order of $1Hz$). In this prototype, the actuation of the wires on the suction side causes bending of the trailing edge towards higher cambered shapes. On the contrary, the actuation of the wires on the pressure side skin causes a decrease in camber. The SMA wires have been studied for decades and an extensive

overview can be found in [12].

The HFVTE actuators are composed of metallic substrates positioned in between Macro Fiber Composite (MFC) piezoelectric patches. The MFC patches are LZT piezoelectric fibers and electrode networks encapsulated within epoxy. When supplied by a voltage, the patches stretch out and generate bending. The Multi-Fiber composite piezoelectric actuators were glued on both sides of a metallic substrate and placed in the trailing edge region. The whole ensemble is covered by a flexible molded silicon in order to retain the trailing edge shape and limit the impact on the actuator's performance. The active length of the HFVTE is $35mm$ chord-wise. This implementation allows for quasi-static tip deformation amplitude of $0.5-1mm$, while able to vibrate retaining large enough amplitudes up to $400Hz$. For further details, related to the design and the electromechanical characterization of the electroactive morphing wing the reader is invited to refer to [13].

2. Experimental procedure

The hybrid morphing wing prototype, as it was mentioned, embeds both camber control and Higher Frequency Vibrating Trailing Edge (HFVTE) actuators. In this analysis however, only the electroactive morphing effects of the HFVTE actuation will be studied. This will highlight the effects coming from the vibrating trailing edge in the context of the hybrid morphing. The present article follows the experimental work of G. Jodin et al. [5] for a Reynolds number of 1 million. The measurements will be compared with the numerical studies following to provide a validation of both approaches.

The wing prototype with a chord dimension of $0.7m$ was placed at an incident angle of 10°in the subsonic wind tunnel S4 of IMFT. The test section has a width of $592mm$ and a height of $712mm$ (see Fig. 1). Time Resolved Particle Image Velocimetry (TR-PIV) measurements will be examined in this paper. The measurement of the unsteady velocity fields by means of TRPIV has been realized with the contribution of the Signal and Image processing service of IMFT (S. Cazin and M. Marchal). The post-processing of the raw PIV results was carried out with the CPIV-IMFT open-source software, de-

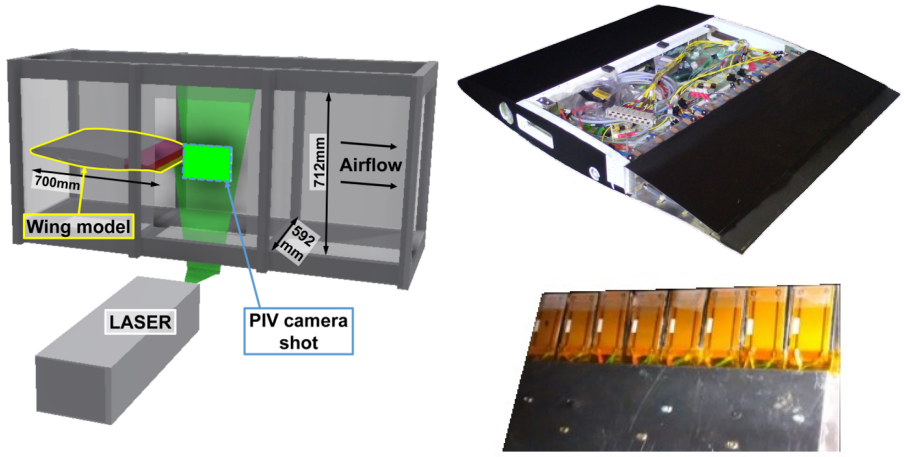

Figure 1: *Schematic representation of the experimental test section of the S4 wind tunnel of IMFT (left) with the Airbus-A320 wing (right-top) mounted on [5]; the prototype bears the HFVTE actuators (right-bottom) on the trailing edge along the span.*

veloped with the contribution of the software services of IMFT (P. Elyakime) for parallel (MPI) post-treatment of the results in supercomputing architectures. This multiplatform (both Windows and Linux platforms) software is based on a multi-grid iterative algorithm with image distortion [14]. It is capable of computing a set of more than 50000 images efficiently in terms of computational time significantly shortening the post-treatment time of large-size results. In the present study, the CALMIP supercomputing center has been used for the data analysis. The software has been successfully validated in comparison with the commercial software DAVIS8 developed by *Lavision*. For a more detailed presentation of the software the reader can refer to to the CPIV Software description online (`http://www.smartwing.org/SMS/EU/CPIV_description`), as the CPIV is used in the context of the European Research programme SMS, "Smart Morphing and Sensing for Aeronautical configurations".

The measurements were carried out at an ambient temperature $(295K)$. The sampling rate was about $10KHz$. For the experimental procedure smoke particles of $3.4\mu m$ diameter were introduced in the airflow, giving a Stokes number $Sk = 5 \cdot 10^{-4}$ which

indicates - as it is sufficiently smaller than 1 - that the particles follow consistently the motion of the fluid. Particle images are recorded during the experiments using the digital high-speed camera Phantom V1210 focused in the mid-section regarding the depth of the field. The laser sheet representation in the mid-span region can be seen placed in the stream-wise direction in Fig. 1. Each image is divided into interrogation windows of $16X16\ pixel^2$ size, which corresponds to $3.4X3.4\ mm^2$, with an overlap of 75%. The thickness of the laser sheet was 2.5 mm. The laser pulsations are generated by a two cavity Nd:YLF (527 nm) laser (Photonics Industries International Inc. DS-527-60) [5] and they were redirected using mirrors to light the wake region right after the wing's trailing edge.

Acquisitions of 50000 images has been proven sufficient to obtain a statistical convergence of the results. The most probable displacement of the particles between two consecutive images is obtained from the cross-correlation plane of consecutive images. The velocity variation evaluated over multiple experiments was estimated to be below 1.5% while the blockage ratio was found to be acceptable as long as the focus is the relative effects of the morphing application. The experimental benchmark was also equipped with an aerodynamic balance in order to measure the lift and drag forces. However, remarking that the quantification of the lift and drag was far from trivial in this study (the measurements were significantly affected by the trailing edge vibration), only qualitative comparisons concerning the morphing effects will be included in this article. For a more detailed description of the experimental equipment and procedure the reader should refer to [5].

3. Numerical approach & turbulence modelling

The time dependent Navier-Stokes equations have been solved under the conservative form in a finite-volume structured grid formulation, using the Navier-Stokes Multi-Block (NSMB) code [15], in both two and three dimensions. The Navier-Stokes equations in 3D Cartesian coordinates, for a viscous perfect gas can be expressed in conservative form as:

$$\frac{\partial}{\partial t}(W)+\frac{\partial}{\partial x}(f-f_v)+\frac{\partial}{\partial y}(g-g_v)+\frac{\partial}{\partial z}(h-h_v)=0$$

where t denotes time. The state vector W is given by:

$$W = (\rho\ \rho u\ \rho v\ \rho w\ \rho E)^T$$

and the convective fluxes are defined as:

$$f = \begin{Bmatrix} \rho u \\ \rho u^2 + p \\ \rho uv \\ \rho uw \\ u(\rho E + p) \end{Bmatrix},\ g = \begin{Bmatrix} \rho v \\ \rho vu \\ \rho v^2 + p \\ \rho vw \\ v(\rho E + p) \end{Bmatrix},\ h = \begin{Bmatrix} \rho w \\ \rho wu \\ \rho wv \\ \rho w^2 + p \\ w(\rho E + p) \end{Bmatrix}$$

where ρ the density, u, v, w the cartesian velocity components, p the pressure and E the total energy. The viscous fluxes are defined:

$$f_v = \begin{Bmatrix} 0 \\ \tau_{xx} \\ \tau_{xy} \\ \tau_{xz} \\ (\tau U)_x - q_x \end{Bmatrix},\ g_v = \begin{Bmatrix} 0 \\ \tau_{yx} \\ \tau_{yy} \\ \tau_{yz} \\ (\tau U)_y - q_y \end{Bmatrix},\ h_v = \begin{Bmatrix} 0 \\ \tau_{zx} \\ \tau_{zy} \\ \tau_{zz} \\ (\tau U)_z - q_z \end{Bmatrix}$$

where τ the shear tensor. The viscous dissipation in the energy equation is calculated from:

$$(\tau U)_* = \tau_{*x} u + \tau_{*y} v + \tau_{*z} w$$

and q_* the hea flux due to conduction calculated according to Fourier's law.

The computational domain is subdivided into a number of quadrilateral (2D) and hexahedral (3D) grid cells resulting in a structured mesh. The multi-block strategy is followed in accordance to the parallelization procedure of the code. A separate discretization of the equations in space and time is applied.

Finite volume cells of constant size in time are considered for the discretization in space. A fourth order standard central skew-symmetric spatial scheme with artificial second and fourth order dissipation terms was used for the convection terms and a second-order central scheme for the diffusion terms. For the temporal discretization, dual time-stepping with a second order implicit backward difference scheme is

performed [16]. The artificial compressibility method was finally chosen after various numerical for the preconditioning of the flow to increase accuracy in the low subsonic regime.

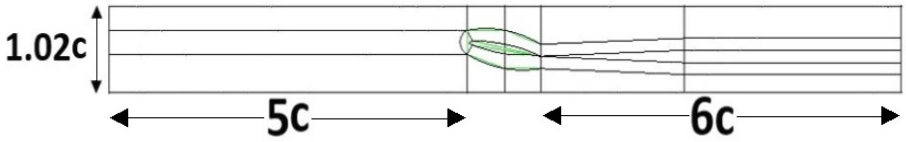

(a) *Multi block description of the computational domain.*

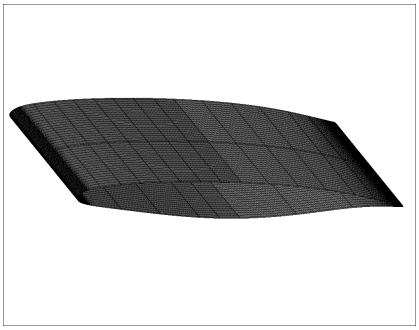

(b) *3D surface meshing of the A320 wing.*

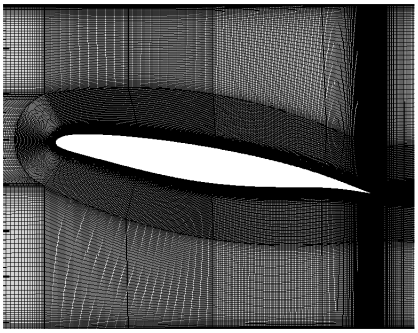

(c) *2D mesh around the A320 wing.*

Figure 2: *Meshing of the computational domain.*

Following the experimental studies carried out in the S4 subsonic wind tunnel of IMFT, computational grids were constructed depicting faithfully the geometry of test section the dimension of which can be found in figure 1. Two meshes M1 and M2 have been used for the 2D computations. The grid sizes were selected after thorough numerical studies. The M1 includes 300000 finite volume cells. The refined version M2 contains 500000 finite volume cells. The points were added in the streamwise direction both on the wing and in the wake region. For the 3D computations the M1 grid was extruded in the span-wise direction leading to a total mesh size slightly higher than 10 million (M3). The y^+ values, corresponding to the first grid spacing above the wall, were below 1 for all the grids considered. A comparison of the results in respect of these three grids will be presented in section 4.2. The three grids are summarized in Table 1.

The physical time-step was kept constant in all the computations at 10^{-5} giving a CFL number around 50. Additional simulations with a Courant number around 5 ($\Delta t = 10^{-5}$) have been performed and the results compared well with the present studies. About $60-80$ inner iterations were carried out for each time-step. The increased number of iterations is justified from the low Mach aerodynamics simulated in the cases following. The upper and lower walls of the tunnel were considered by means of both non-slip (zero velocity at the wall) and slip (velocity tangent to the surface) boundary conditions. After numerical tests that indicated no considerable effect due to the respective boundary layers on the wake development, the simulations were carried out with the slip boundary conditions, providing a better agreement with the experimental results. A velocity inlet and a pressure outlet were used in the respective boundaries of the domain. The boundary conditions and the computational parameter has been chosen after various numerical tests. For the morphing test cases, where the body dynamically deforms, the unsteady Arbitrary Langrangian Eulerian (ALE) methodology [17] was used for the moving grid by taking into account the convection of the grid nodes during the deformation. A second-order polynomial was used for the calculation of the imposed deformation of the wing's surface.

Grids	**2D**	**3D**	**Cells**
M1	✓		300K
M2	✓		500K
M3		✓	10M

Table 1: *Grids developed for the numerical analysis.*

In the present work the Organized Eddy Simulation (OES) approach [18], [19], [20] has been employed for the turbulent flow. Based on the ensemble (phase) averaging of the flow, this approach is sensitized to allow coherent structures and their related instabilities to develop in the high Reynolds number range and is well adapted for detached flows, both typical of all aeronautical applications. The OES approach is non-inherently 3D and therefore can be applied in 2D simulations with sufficient accuracy in capturing the main coherent structure dynamics and their modification. Therefore,

it provides a robust method for capturing physical phenomena and treating near wall turbulence. The turbulent transport equations added are the ones used in the $k-\varepsilon$ model ($k-\varepsilon-OES$) where the closure coefficients, the dumping functions and the surface boundary conditions have been reconsidered based on statistical turbulence modeling and on the modified turbulent scales. A more detailed description of the OES can be found in [18] and [19].

4. Static case: experimental and numerical results

In this section both numerical and experimental results of the non-morphed wing are examined. For all the results following the wing is mounted with an incidence angle of 10°. The chord of the prototype was constant and equal to $0.7m$. The incoming velocity was held constant $(21.5m/s)$ which for the reference values of temperature $(293K)$ and pressure $(101325Pa)$ gives a Reynolds number of 1 million. The turbulence intensity of the inlet section of the wind tunnel was estimated at about 0.1% of the free stream velocity. For the numerical simulations, a higher value (close to 1%) was used. Due to the dissipation transport equation, a significant decay of turbulent kinetic energy occurs from the inlet section towards the whole computational domain. Increasing the freestream turbulence intensity ensures a significant distance between the inlet boundary and the body, allowing for a more faithful representation of the experimental test section, and at the same time providing comparable turbulent intensities with the experiments around the body.

4.1. Time resolved PIV results

The instantaneous velocity field measured by means of TRPIV is presented in Fig. 3. The plane presented in this figure is the one right after the wing, as presented in 1. The stream-wise direction for the measurements is on the x axis and the vertical direction is that of the y axis. The $y/c=0$ value corresponds to the position of the trailing edge. Numerical points were added in post-processing to follow the velocity vector measured at each time-step, providing a streakline visualization. In that sense, the color of each ”particle” represents its initial positions. With the streakline visualization, the

coherent and chaotic turbulent structures developed in the wake are highlighted providing a view of the dynamic behavior of the wake. The turbulent wake is restrained in between two interfacial thin shear layers, the Turbulent/Non-Turbulent (TNT) Interfaces [21], [22]. Well inside the wake region, additional Turbulent/Turbulent Interfaces develop [23]. The interfaces are clearly exhibited in Fig. 3 as captured by TRPIV measurements and indicated with the respective notation.

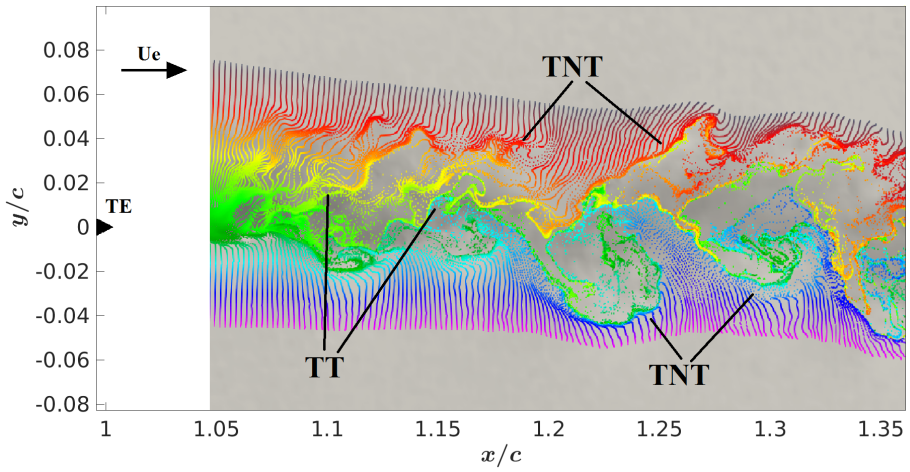

Figure 3: *Instantaneous velocity field from the TRPIV measurements, visualizations by means of streaklines for* $Re = 1M$*, angle of attack* $a_o = 10°$*; trailing edge marked with a symbol; the color of each particle represents its initial positions.*

At a given camber, the vibrating trailing edge is expected to create small-scale turbulent eddies and to add kinetic energy in the wake, which in turn causes interactions in the upper and lower shear layer. This aims at enhancing the supercritical character of the flow and producing an eddy-blocking effect constricting and strengthening (shielding) the shear layers and achieving narrower wakes [5].This shear sheltering effect produced, leads to a considerable thinning of the separated shear layers, as shown in [19]. The thinning of the wake region as well as feedback effects through the vorticity, enable simultaneous increase of lift and decrease of noise sources. This eddy-blocking concept was first studied numerically in [19] for a transonic flow around a supercritical airfoil and put in evidence experimentally thanks to the electroactive morphing [24].

In the present study, the flow field right after the supercritical wing is accessible due to the TRPIV measurements, and the same phenomena will be exhibited as achieved by the HFTEV actuating morphing system.

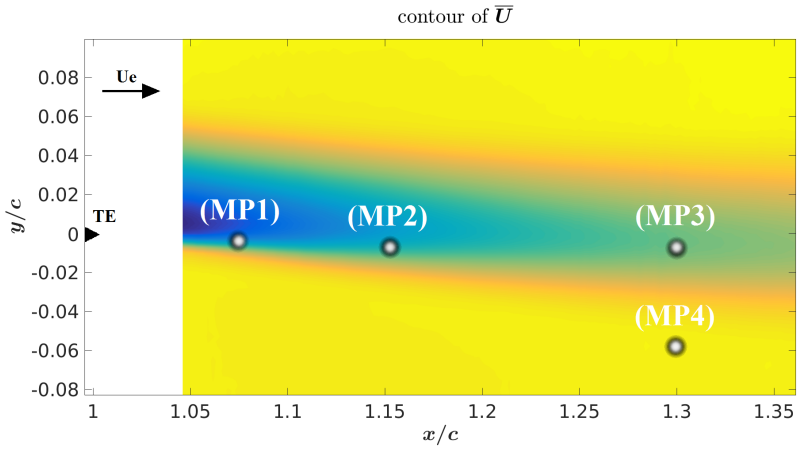

(a) *Contour of time-averaged longitudinal velocity from TRPIV measurements; position of the monitor points along the wake; the trailing edge is marked with a symbol.*

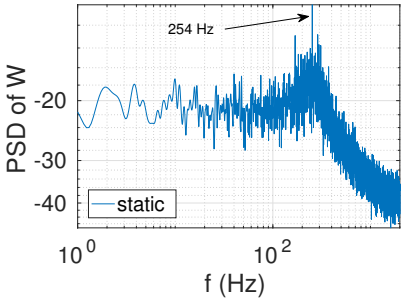

(b) *Spectrum from monitor point 2.*

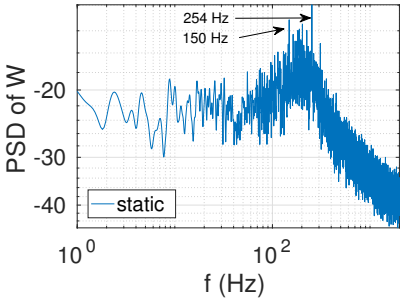

(c) *Spectrum from monitor point 3.*

Figure 4: *Spectral content of the vertical velocity component in the near wake region; TRPIV results for the static case.*

To further investigate the dynamics in the static configuration case (no morphing applied), temporal signals of the vertical velocity component have been extracted in selected positions downstream of the trailing edge and the corresponding Fast Fourier Transforms (FFT) of these signals have been calculated. Plots of the Power Spectral

Density are presented in Fig. 4b and Fig. 4c for two points selected in the near wake region (see Fig. 4). The predominant frequency bump shown in these spectra corresponds to an alternating shedding mode developed downstream. The bump's existence is representative of a coherent pattern smeared by chaotic turbulence motion caused by non-linear interactions between the coherent vortex shedding and the finer scale chaotic turbulent motion. This irregular formation of large scale structures is characteristic of the supercritical flow developed in this Reynolds range.

The characteristic frequency of the Kármán instability is found to be around 254 Hz as indicated by the signal acquired from monitor points 2 and 3. This frequency corresponds to a Strouhal number between 0.4-0.5 (for a characteristic length equal to the initial wake's width) which is in agreement with measurements for circular cylinders close to the same Reynolds number [25]. The instability is a result of the interactions between the lower and upper shear layers, developed from the respective unstable boundary layers. Traces of these shear layer instabilities can also be spotted in the spectra. The lower shear layer instability is placed in a higher frequency range (around 380 Hz) while the upper shear layer seems to be placed around 150 Hz.

A detailed study of the PIV measurements by a Proper Orthogonal Decomposition (POD) is included in [5] and allows distinguishing the coherent from the chaotic effects.

4.2. Numerical study

The numerical simulations have been carried out respecting the aforementioned experimental conditions. The grids were constructed depicting faithfully the geometry of test section. For the numerical simulations, the stream-wise direction is on the x axis and the vertical direction is that of the z axis, leaving y axis along the span-wise direction. This is the reference system that will be used for the comparison of the computations with the experimental results. Unlike the experimental reference system, here the $z/c = 0$ value corresponds to the position of the leading edge. For the validation of the static case, 3D and 2D simulations were carried out. For the morphing tests that follow, only a two-dimensional study has been carried out, allowing an extensive multi-parametric study in order to assess the optimal frequency and amplitude ranges - in respect of the aerodynamic performance - with reasonable CPU time.

As it will be shown, the comparison between 3D and 2D simulations justify using a two-dimensional parametric study in order to describe the morphing effects.

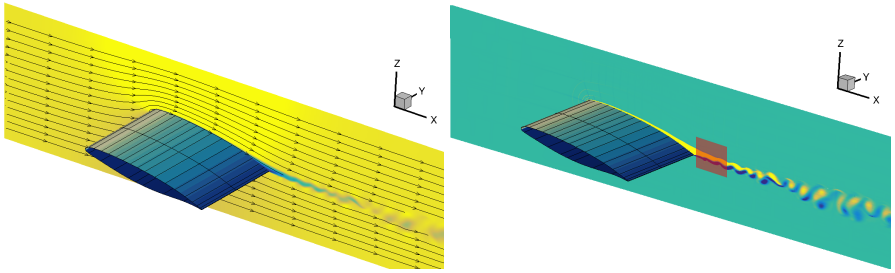

(a) *Velocity magnitude on a plane section.* **(b)** *y vorticity component on a plane section.*

Figure 5: *3D simulation for* $Re = 1M$*, angle of attack* $a_o = 10°$*, contours of time averaged surface pressure on the wing.*

Figures 5 provides a global view over the computational domain and the solution acquired by means of numerical simulation with the M3. The flow coming from the inlet moves downstream from left to right from hereby after. In Fig 5b the plane used for the PIV measurements is represented with a rectangular box, defined for all comparisons between computed and measured data that follow. A small detachment at the trailing edge of the wing is evident through streamlines in Figs. 6 and 8b resulting to the unstable wake region following right after. The detachment leads to a thicker effective body and an unstable wake region. The upper and lower shear layer instabilities interact with each other giving an irregular alternating shedding further downstream. This gives birth to secondary three-dimensional instabilities by mechanisms studied and explained in low Reynolds numbers around a wing in [26].

Figure 6 illustrates the formation of undulated vortex rows along the span, displaying large-scale wavelengths. The coherent vortices develop spanwisely counter-rotating cells according to a secondary instability amplification as studied in [27] and become undulated displaying predominant wavelengths that are fractions of the chord (Fig. 7). Despite this three-dimensionnality, the mean velocity profiles are close to the ones simulated in 2D (Fig.11).

Contours of the time-averaged velocity magnitude and the instantaneous turbulent

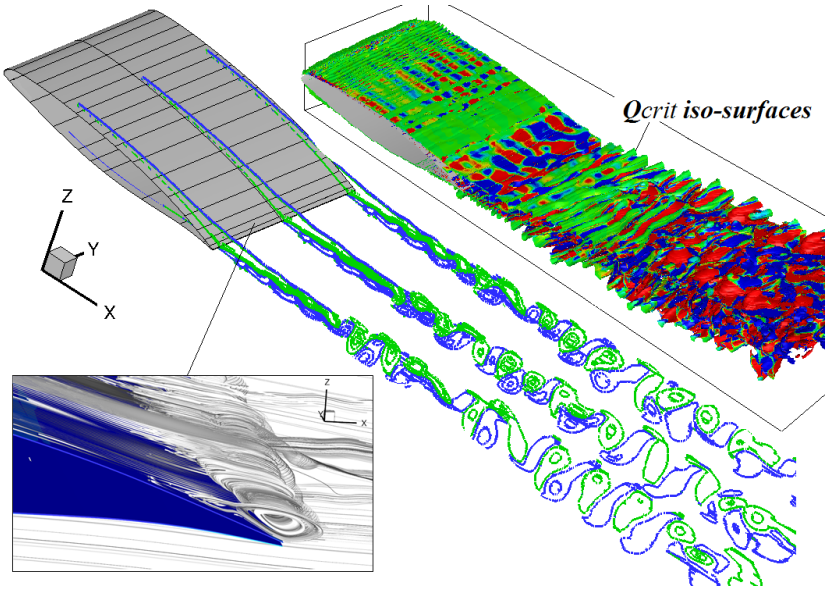

Figure 6: *Results from the 3D simulation for* $Re = 1M$*, angle of attack* $a_o = 10°$*. Birth and evolution of the primary and secondary instabilities in the wake; in the middle iso-lines of span-wise* (y) *vorticity component along the near wake region; Q criterion iso-surfaces colored by longitudinal vorticity ranging from* $[-2]$ *(blue) to* $[+2]$ $1/s$ *(red).*

kinetic energy k calculated by means of numerical simulation with M1 are presented in Fig. 8. The regions close to the leading and trailing edge respectively are zoomed. The quasi-steady detachment begins after $x = 0.55$ which corresponds to an $x/c \approx 80\%$. Close to the leading edge, the appearance of a laminar separation bubble guides after re-attachment the transition to turbulence as depicted in Fig. 8c. The production of turbulent kinetic energy starts only after $x = 0.03$ which corresponds to an $x/c = 4.3\%$ and as a result, the boundary layer at the separated trailing edge is turbulent. The unstable upper and lower boundary layers can be viewed in Fig. 8d.

It has been shown (Fig. 6) that the flow has a pronounced 3D character. However, the initial development of the vortical patterns in the wake has a strong apparent two-dimensional behavior. As a result, the main flow dynamics involved in the wake development can be accurately captured even by the standard 2D mesh (M1) and are in

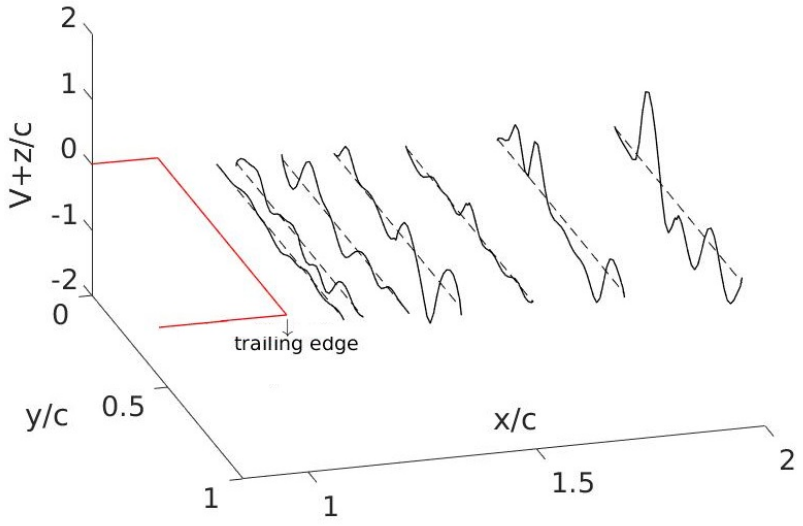

Figure 7: *Spanwise velocity component along the wake by means of numerical simulation; the 3D effects result to spanwise predominant wavelengths that are fractions of the chord.*

good agreement with the experimental ones. Figure 9 attests to this. The width of the spectral bump is well captured both close to the trailing edge and further downstream in the wake where the alternating shedding is fully developed. Spectral peaks underline the main instabilities in the wake. The vortex structure dynamics and their non-linear interactions can be visualized using streaklines in the wake, pictured in Fig.9a.

The unstable shear layers develop global predominant frequencies close to the trailing edge. As seen in the experiments, the lower and upper shear layers interact with each other yielding a von Kármán vortex street further downstream. The vortex shedding is placed around 214 Hz, which compares well with the value obtained from the experiments. The unstable upper shear layer seems to present oscillation around 170 Hz while the lower shear layer is characterized by a higher frequency (above 370 Hz), also in relative agreement with the PIV measurements. All the above mentioned frequencies will be referred to from hereby and after as natural frequencies as they correspond to instabilities that appear naturally in the flow. These effects are also highlighted

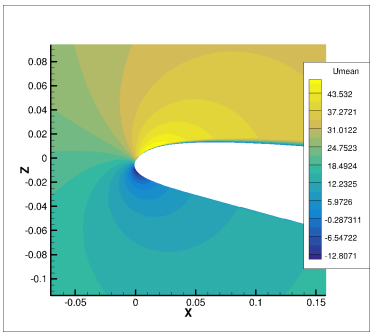

(a) *Time averaged velocity magnitude close to the leading edge.*

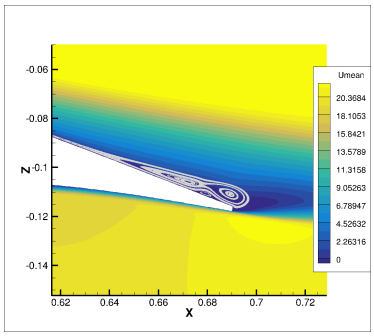

(b) *Time averaged velocity magnitude close to the trailing edge.*

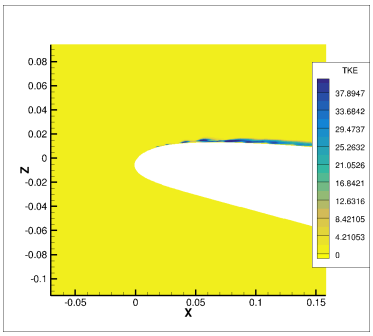

(c) *Ensemble-averaged turbulent kinetic energy close to the leading edge.*

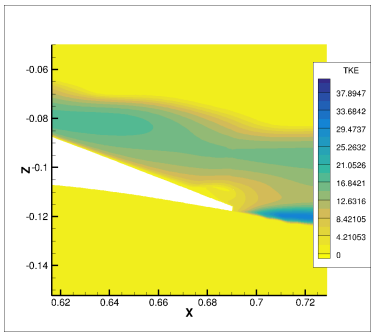

(d) *Ensemble-averaged turbulent kinetic energy close to the trailing edge.*

Figure 8: *Contours of velocity and turbulent kinetic energy, 2D simulation with M1 grid for* $Re = 1M$*, angle of attack* $a_o = 10°$*; the detachment is represented by streamlines close to the trailing edge.*

by the Proper Orthogonal Decomposition performed on the computational results and presented in later section of this article.

In figures 10b and 10c some characteristic wake values are presented, comparing the various numerical tests to the experiments. The calculation for the displacement and momentum thickness in the wake follows eq. 1 and 2, where $u_{99\%} = 0.99 \cdot U_{inlet}$ and $z^*_{99\%}$ the vertical positions along the wake where this is achieved. The superscript

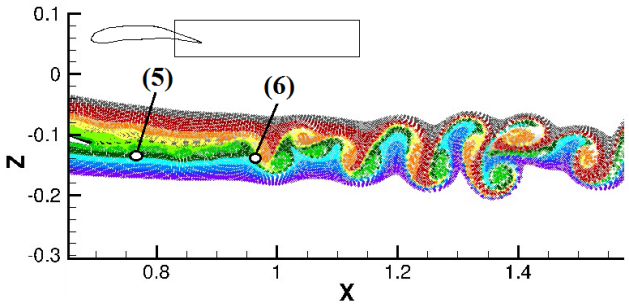

(a) *Position of the monitor points in the computational domain along the wake; trailing edge tip at* $x = 0.69$*; streaklines where the color of each particle represents its initial positions.*

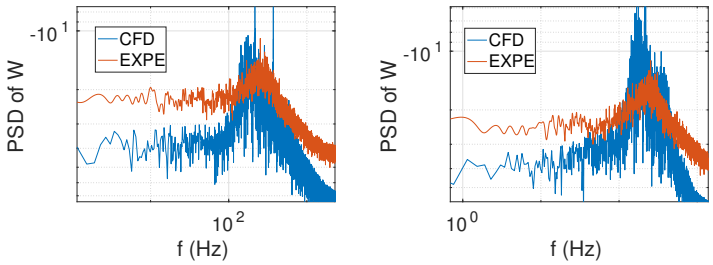

(b) *Spectrum from monitor point 5.* **(c)** *Spectrum from monitor point 6.*

Figure 9: *Spectral content of the near wake region, comparison between computational results for the M1 grid and experiments,* $Re = 1M$*, angle of attack* $a_o = 10°$.

low and *up* refer to the lower and upper shear layer position respectively.

$$\delta^* = \int_{z_{99\%}^{low}}^{z_{99\%}^{up}} (1 - \frac{u}{u_{99\%}}) dz \tag{1}$$

$$\theta = \int_{z_{99\%}^{low}}^{z_{99\%}^{up}} \frac{u}{u_{99\%}} (1 - \frac{u}{u_{99\%}}) dz \tag{2}$$

The displacement thickness δ is accurately predicted with the three different grids. The momentum thickness, closely related to the forces, presents a better agreement for the refined mesh M2. Additionally, comparisons of the time averaged velocity profiles along the wake are depicted in figures 10a and 11. Extracting and comparing the

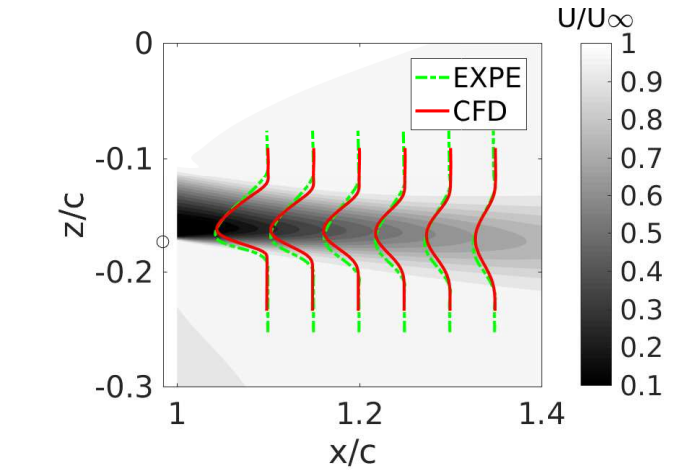

(a) *Time averaged axial velocity profiles; comparison between the computations for the M1 grid and the experimental results; trailing edge marked with a symbol.*

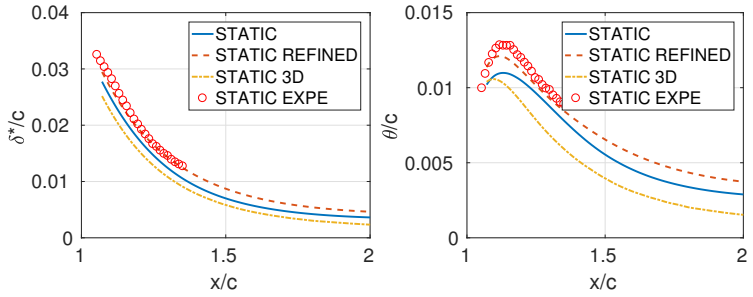

(b) *Displacement thickness.* **(c)** *Momentum thickness.*

Figure 10: *Quantitative comparison of the computational test with the TRPIV results (STATIC EXPE); numerical tests for: M1 mesh (STATIC), the refined M2 mesh (STATIC-REFINED) and M3 mesh (STATIC 3D).*

velocity profiles for various x/c non-dimensional positions, it is evident that the agreement between the measured and computed profiles is quite satisfactory for all the grids tested.Despite the aparent three-dimensional character of the flow, the focus in the 2D simulations for the overall investigation and the morphing results in the present study is well justified. It is reminded that the reference system is the one used in the simulations. The wake expansion is accurately captured and only at the latest position the

velocity deficit is slightly overestimated. After the various comparison it is evidenced that both the dynamic and the mean characteristics of the flow are well captured even with the M1 grid.

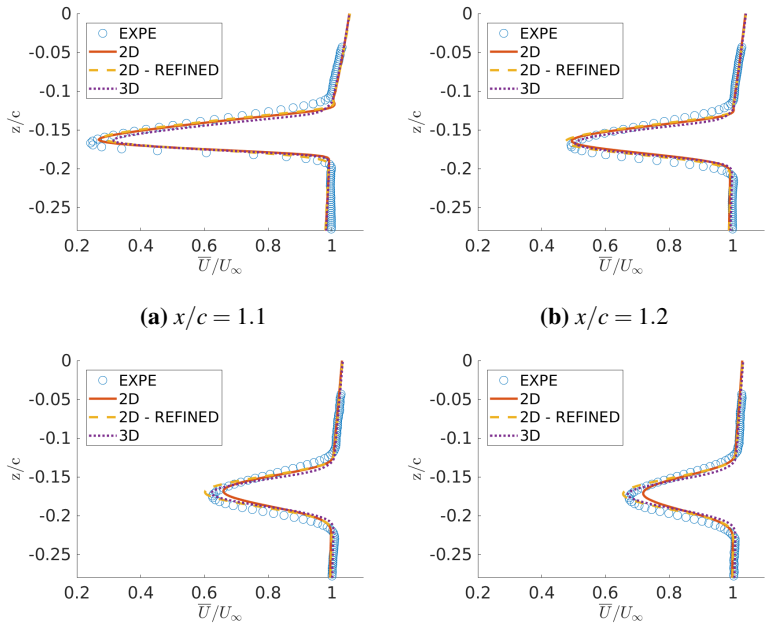

(a) $x/c = 1.1$ **(b)** $x/c = 1.2$

(c) $x/c = 1.3$ **(d)** $x/c = 1.35$

Figure 11: *Comparison of axial time averaged velocity profiles along the wake for $Re = 1M$, angle of attack $a_o = 10°$; computational tests for the M1 mesh (2D), the refined M2 mesh (2D-REFINED) and the M3 mesh (3D) compared with the TRPIV results (EXPE).*

5. Dynamic case: electroactive morphing near trailing edge

The HFVTE system on the prototype is designed to reach amplitudes up to one millimeter. The technical characteristics for the electro-active hybrid morphing actuation are extensively described in [4] and [13]. The motion and slight deformation of the near-trailing edge region due to the $L_p = 35mm$ long MFC piezo-actuators vibrating is also applied in the numerical simulations. This section includes both experimental and

computational results in that order, following the same organization with the previous section.

5.1. Experimental analysis of the morphing

For the investigation of the morphing results a different window for the TRPIV measurements will be studied. The image acquisition takes place at a region that includes the trailing edge. The morphing frequency will be increased progressively and the changes in the dynamics will be then compared with the numerical investigation that follows. Visualizations by steaklines will be examined to attest to the different flow structures witnessed due to the high frequency vibration applied on the trailing edge. As mentioned in a previous section, the streaklines presented in Fig. 12 are produced by adding numerical points in post-processing but this time, blue seeds are emitted from the pressure side while red ones from the suction side covering the respective boundary and shear layers. Black colored seeds used in the first and last figure are placed close to the separation point in order to highlight possible sharp turbulent-turbulent interfaces. The results presented in Fig. 12 correspond to a $Re = 500000$ allowing only for a qualitative comparison with the numerical computations carried out for a higher Reynolds number.

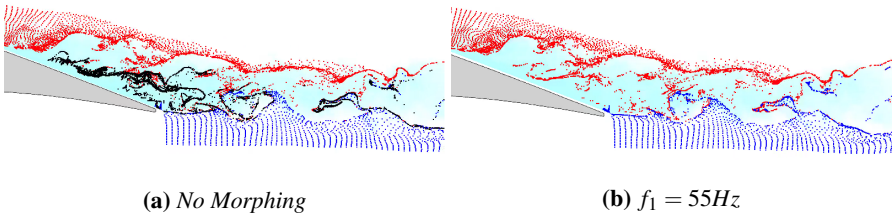

(a) *No Morphing* **(b)** $f_1 = 55Hz$

(c) $f_2 = 110Hz$ **(d)** $f_3 = 220Hz$

Figure 12: *Development of vortical structures in the wake, visualization with streaklines, TRPIV measurements for various actuating frequencies.*

The non-actuated case (Fig. 12a) will serve as a reference and then the morphing frequency will be varied taking increasing values (i.e. $0 < f_1 < f_2 < f_3$). The frequencies presented in Fig. 12b- 12d are sufficiently spaced and each of them is specifically selected as it prompts different effects in the wake. Starting at a low frequency $f_1 = 55Hz$ no apparent effects in the coherent wake dynamics are visible. Moving to a higher frequency $f_2 = 110Hz$ leads to a change in the modes in the wake (Fig. 12c) as the natural shedding frequency is approached. An alternating pattern is formed and a von Kármán sheet is shaped right after the wing tracking the actuation frequency. This will be observed also in the simulation where the actuation frequencies are shifted to higher values, conformal to the increase of the natural frequency due to the higher Reynolds number (1 million). Finally, applying an even higher frequency $f_3 = 220Hz$, the dynamics change once more. The lower shear layer instability gets reinforced as its natural frequency is approached by f_3 and is locked to the actuation frequency as it can be seen in Fig. 12d. Energetic smaller vortices are convected downstream, the upper shear layer instability seems to be blocked in regards to how it affects those vortices and the wake remains thin as it depends on the size of the newly created turbulent structures.

An explanation of the mechanisms involved is attempted here. To this end, the black color seeding added to the non-morphed (Fig. 12a) and last actuation case (Fig. 12d) can be of help. As the upper and lower seeding can demonstrate the turbulent / non-turbulent (TNT) interfaces, the black seeding seems to follow an existing turbulent / turbulent interface (TT) that manifests itself due to the shear caused by the detachment of the flow. This interface is manipulated by the morphing applied on the trailing edge and is hypothesized that could aid to the shielding of the shear vortices created in that it provides a thin layer that de-correlates the two TNT interfaces. It has been proven in [23] that interfacial shear layers tend to act in this way. It is possible that this interface strengthens the low shear layer vortices with which it seems to correlate, blocks the interactions and perturbations coming from the upper shear and helps them propagate unaltered downstream. This could as well be a clear manifestation of eddy blocking phenomena taking place and preventing the generation of larger turbulent structures in the wake (as in the static case). The way this interface acts and guides the dynamics

when an alternating pattern is established remains to be investigated.

5.2. *Numerical investigation of the morphing*

The Arbitrary Lagrangian-Eulerian methodology [17] is utilized for the calculation of the variables in the deformable/moving grid. The applied displacement in the trailing edge region follows exactly the second-order polynomial deformation applied on the reduced scale prototype. The frequency of the vibration f_a and the amplitude A_o of the sinusoidal time variation are left to be imposed in each test case. The time variant polynomial vertical deformation dz for every surface point along the streamwise x direction, is given in Eq. 3.

$$dz = A_o[\frac{2}{3{L_p}^2}(x-x_o)^2 + \frac{1}{3L_p}(x-x_o)]sin(2\pi f_a) \tag{3}$$

for every $x > x_o$, where $x_o = c - L_p$ with c the chord of the airfoil and L_p the patch length (equal to $35mm$ in our application).

The amplitude corresponds to the maximum displacement, i.e. the displacement of the ending tip of the trailing edge. In the tests following, the effect of the aerodynamic forces on the vibrational behavior of the piezo-actuators has not been taken into account (one-way fluid-structure interaction) since they have been evaluated as negligible in [13]. For this section, the effects using only the M1 grid will be examined as it has been proven to provide results that compare well with the experimental data and will enable a multi-parametric study due to the reduced computational cost. This will provide a complete image over the morphing effects achieved with the HFVTE system. The Reynolds number for the numerical investigation of the morphing effects was 1 million, as for the static case.

5.2.1. *Effects on the wake dynamics*

The morphing has prominent effects on the development of vortical structures in the wake. The amplitude of the vibration was held constant at $0.35mm$ while different values for the actuation frequency f_a were tested. This amplitude value was chosen as it was the largest one to be tested during the first series of experiments with this specific morphing implementation. Visualizations by streaklines created in the same

manner with the experiments, are presented in Fig. 13, comparing the effects due to the sinusoidal actuation (figures 13b- 13d) with the case where no morphing was applied (Fig. 13a). Respectively, in Fig. 15 contours of the ensemble-averaged y vorticity component (axis vertical on the plotted plane) highlight the morphing alterations of the dynamics in the wake for various frequencies.

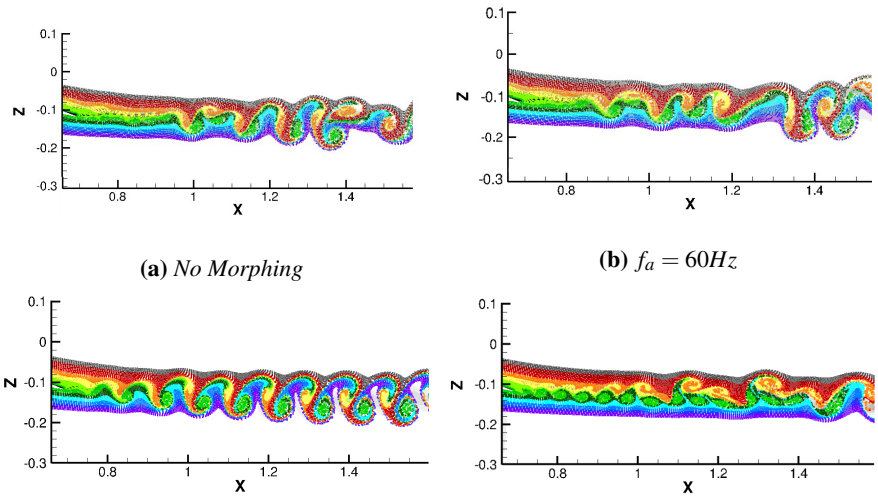

(a) *No Morphing* **(b)** $f_a = 60Hz$

(c) $f_a = 200Hz$ **(d)** $f_a = 300Hz$

Figure 13: *Development of vortical structures in the wake by means of numerical simulation, visualization with streaklines; the color of each particle represents its initial positions. The amplitude is* $0.35mm$ *for every actuating frequency.*

For frequencies lower than the ones related to the shear layer instabilities and the alternating shedding (e.g. for $f_a = 60Hz$), the flow coherent dynamics seem unaffected by the perturbation travelling at a much lower propagation speed, in accordance with the experimental investigation. For an actuation close to the von Kármán shedding frequency $(f_a = 200Hz)$, resonance phenomena take place. As seen also in Fig. 12c, the alternating vortex shedding "locks" onto the morphing frequency, non-linear interactions are suppressed and large coherent, highly energetic structures are developed creating clearly a vortex sheet. This was first suggested in [10] where the receptivity of the flow in the wake of an airfoil was studied. It was proven that for a frequency

range (namely the "locking range") around a natural frequency the measured velocity signals presented a uniform time series, a suppression of irregularities and an energy increase of the fluctuations. The width of this range was dependent on the amplitude of the input power of the forcing.

By further increasing the actiation frequency ($f_a = 300Hz$), smaller vortices are generated in the lower shear region and get convected further downstream. These vortices of high momentum are reinforced and shielded due to the morphing and as a result they tend to remain intact ignoring the influence of the upper shear layer. The interaction with the latter is downgraded resulting to the suppression of the alternating sheading until way further downstream. The forced lower shear layer undergoes a merging process that leads to the halving of its frequency and an alternating pattern emitted at this halved frequency after $x = 1.4m$. As a result, the wake regions remains much thinner for a longer distance after the wing.

This behavior is highlighted in the spectra plotted in Fig. 14 where the Fast Fourier Transformation (FFT) of the vertical velocity signals is computed. The signals are acquired for the same point in the wake for various morphing cases. For lower actuating frequencies (figures 14a and 14b) the spectral content of the non-morphed case seems almost unaffected. The frequencies naturally existing in the flow continue to guide the formation of vortices. The energy of the actuation is not receipted by the flow and the power of the morphing frequency remains in low levels. In contrast, for the higher frequencies tested (figures 14c and 14d) the wide bump seen in the static case is replaced by a redistribution of the flow's energy in the harmonics of the actuation frequency. The natural frequencies are suppresed and replaced by these harmonics.

A more complete image of the way the morphing affects the dynamics in the wake region can be deducted considering Fig. 15. Snapshots of the ensemble-averaged y vorticity contours are extracted to highlight the vortical structures produced in the wake. Due to the nature of the turbulent spectrum, it is interesting to go over the morphing effects by sweeping over a wider range of frequencies. For $f_a = 100Hz$ (same for the $f_a = 60Hz$ which is ommited here) similar remarks as previously can be made. No apparent effect in the dynamics is visible and the irregular character of the flow is prevailing. Applying the morphing at $f_a = 150Hz$ and approaching the upper shear layer

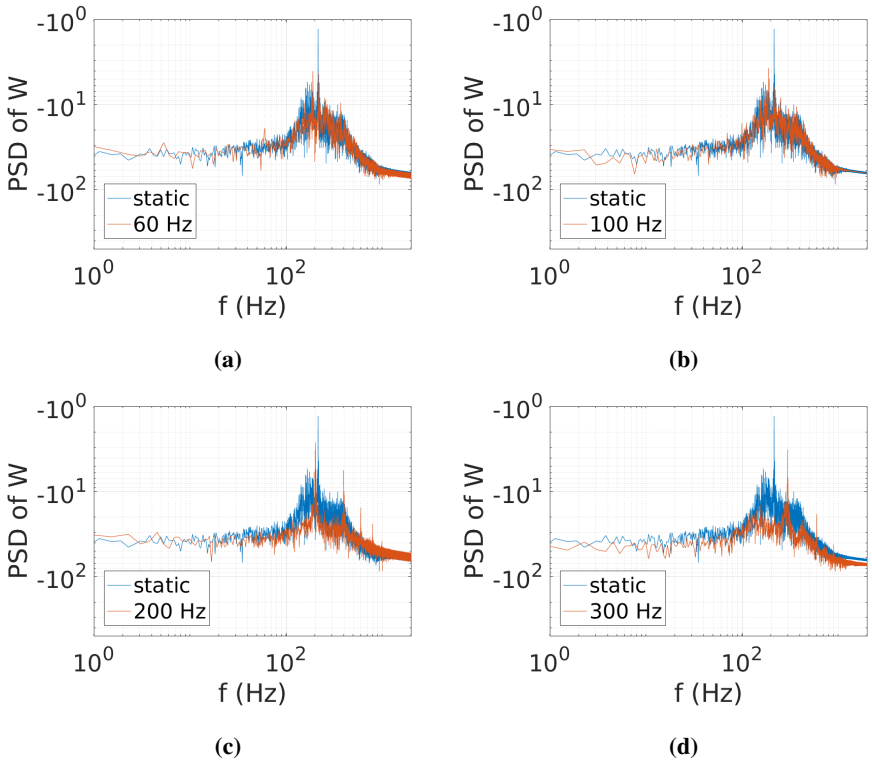

Figure 14: *Spectra of the vertical velocity profile in the wake by means of numerical simulation; the case where no morphing is applied (STATIC) in blue is plotted versus various actuating frequencies.*

instability, it becomes enhanced and takes over leading to a regular alternating pattern immediately after in the wake that tracks the forcing frequency. Increasing the f_a further away from the spectral bump of natural frequencies weakens the "locking mechanism" and irregularities start to reappear closer to the wing. Actuating at $f_a = 450Hz$ brings back the "lock-in" phenomena probably acting as the harmonic of a natural frequency. However, the wake region remains thinner as smaller faster structures are developed. Further increasing the frequency once again leads to a change in the flow mode, the low shear layer gets mainly affected and guides the wake development.

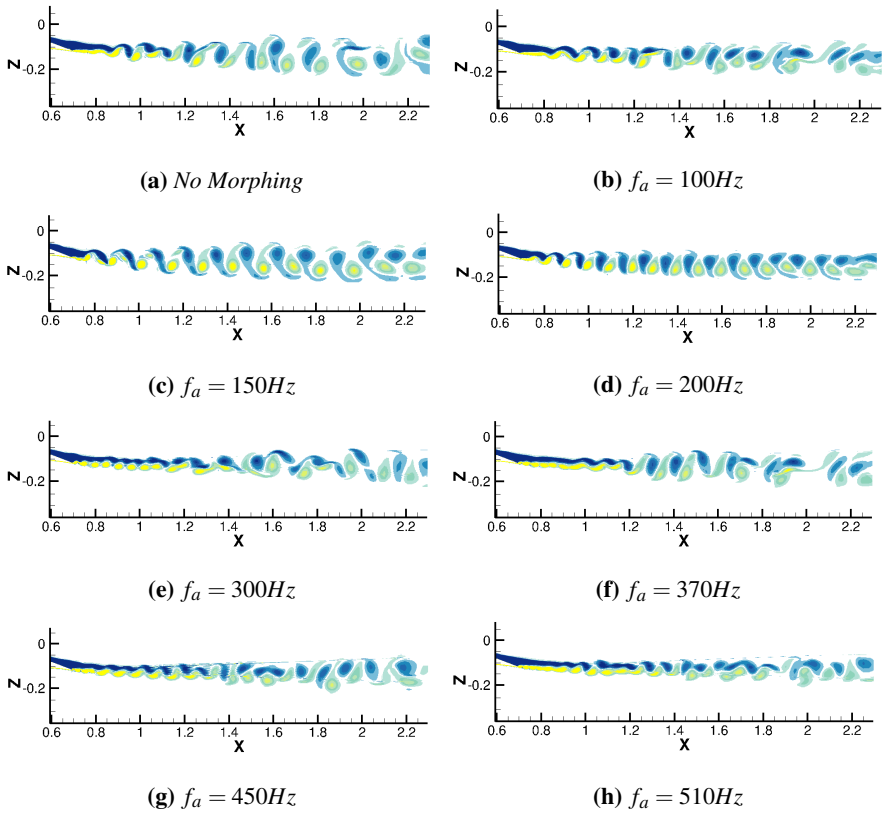

(a) *No Morphing* **(b)** $f_a = 100Hz$

(c) $f_a = 150Hz$ **(d)** $f_a = 200Hz$

(e) $f_a = 300Hz$ **(f)** $f_a = 370Hz$

(g) $f_a = 450Hz$ **(h)** $f_a = 510Hz$

Figure 15: *Development of vortical structures in the wake, visualization with the ensemble-averaged y vorticity component, calculation by means of numerical simulation. The amplitude is set at* 0.35*mm for every actuating frequency.*

5.2.2. POD analysis

The Proper Orthogonal Decomposition (POD) is applied here for the eduction and study of the coherent structures developed in the flow. The POD method was introduced first by Karhunen and Loweve and applied in Fluid Mechanics by Berkooz et al. [28]. The flow field solution is split in spatial modes and temporal coefficients sorted by their importance (relative energy) in the flow. The tempo-spatial evolution of a flow variable U can be expressed as:

$$U(\mathbf{x},t) = \overline{U}(\mathbf{x}) + u'(\mathbf{x},t) = \overline{U}(\mathbf{x}) + \sum_{n=2}^{N} \alpha_n(t)\Phi_n(\mathbf{x}) \tag{4}$$

i.e. as the summation of the decoupled coefficients a_n and Φ_n varying only temporally or spatially respectively. The $\overline{U}(\mathbf{x})$ denoted the time averaged U while the $u'(\mathbf{x},t)$ corresponds to the fluctuating part of the flow variable. The Snapshot POD methodology is applied here on the computational results for the two components of the velocity field. In this way there is a direct correspondence between the eigenvalues provided by the method and the kinetic energy of the flow. Two cases are examined here: the static one where no morphing is applied and the actuation at $300Hz$ where we have prominent effects in the wake development and a change in the nature of the flow modes. In both cases the sampling rate was taken constant ($10^{-4}sec$) and a series with the same number of successive snapshots (619) was used to construct the POD data matrix, providing a time duration that covers multiple periods of the flow phenomena.

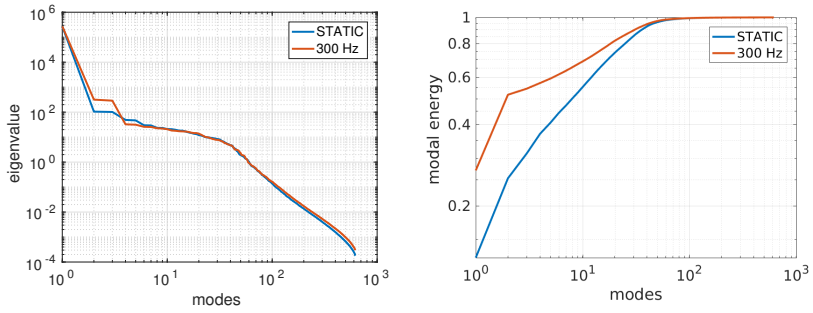

(a) *Sorting of eigenvalues.*

(b) *Relative fluctuating energy.*

Figure 16: *Eigenvalues of the modes sorted by the method (left) and relative cumulative energy (right) corresponding only to the fluctuating part of the flow, predicted by means of numerical simulation.*

In Fig. 16a the eigenvalues of the respective modes are plotted for the two cases. The first mode corresponding in the mean flow, exhibits the highest values as it represents the biggest portion of the flow's kinetic energy. Modes with higher order have smaller relative importance and they represent an increasingly diminished part of the energy of the flow. Taking into account the modes corresponding only to the fluctuating part of the flow (Fig. 16b) it can be deduced that less than 60 modes cover 98% of the fluctuating energy. Due to the high Reynolds number and the irregular dynamics

the energy of the flow is spread over multiple modes. The energy levels of the first few fluctuating modes are increased in the morphing case and the slope of the cumulative fluctuating energy is reduced attesting to the weakening of flow irregularities and the reinforcement of the first modes dynamics. While the energy of the mean modes is in the same level (less than 1% difference) between the two cases, the total fluctuating energy is significantly increased in the morphing case as highly energetic modes are developed due to the receptivity of the flow to the morphing.

The spatial as well as the temporal behavior of the modes is significantly different between the two cases as it was expected from previously discussed results. This is exhibited in figures 17 and 18 where the spatial distribution of selected modes is plotted in the wake region. The modes coming from the horizontal and the vertical velocity components are noted as U_n and W_n respectively, where n denotes the order of the mode. Alongside, the FFT of the respective temporal coefficient of each mode is also presented to provide a correspondence to the frequency analysis that preceded.

For the case where no morphing is applied (Fig. 17), the modes 2 (coupled with mode 3) and 4 (coupled with mode 5) correspond to the initial instability and the alternating shedding respectively, as they have been evaluated in the spectral analysis. Mode 6 presents modulations of the shedding due to non-linear interactions and irregularities. Higher modes (not presented here) also correlate with modulations and low frequency feedback effects. Mode 27 indicates the shear layer instability pattern. A frequency close to $350Hz$ prominent in this region is interacting with the shedding frequency also visible in the spectrum. This instability could be related to a separation bubble created on the pressure side, close to the trailing edge, due to the (supercritical) shape of the A320 wing. Modes of even higher order (above 50) are related to smaller scale fluctuations in the wake that present a more chaotic nature.

Considering the morphing case (Fig. 18) the following modifications are present. Mode 2 (coupled with mode 3) corresponds to the reinforced shear layer close to the trailing edge. The temporal coefficient presents a development locked at the actuating frequency ($300Hz$) while the spectrum of mode 4 (coupled with mode 5) related to the secondary instability takes place at a frequency with half of this value. In this case, the von Kármán shedding takes over only further downstream and is contained to a

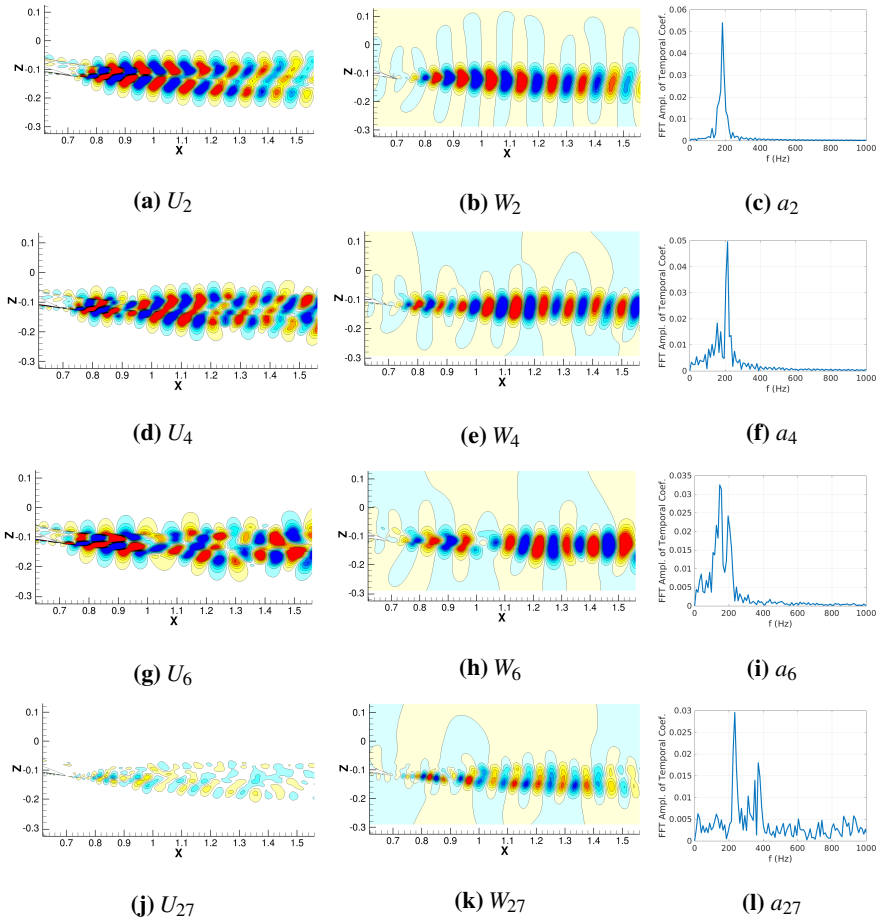

(a) U_2 **(b)** W_2 **(c)** a_2

(d) U_4 **(e)** W_4 **(f)** a_4

(g) U_6 **(h)** W_6 **(i)** a_6

(j) U_{27} **(k)** W_{27} **(l)** a_{27}

Figure 17: *Spatial modes computed with the POD corresponding to the two velocity components and FFT of the respective temporal coefficients. Indices provide the order of the mode; the first (mean) mode is omitted. Case without morphing by means of numerical simulation.*

less wide region as the whole wake becomes thinner. This change in the wake form is directly associated with the enhancement of the aerodynamic performance analysed in a following section. Modulations of the instabilities occur, indicating however a move to different and narrower frequency range (Mode 6) while harmonics of the actuation frequency appear as well in higher modes (not presented here) causing further interac-

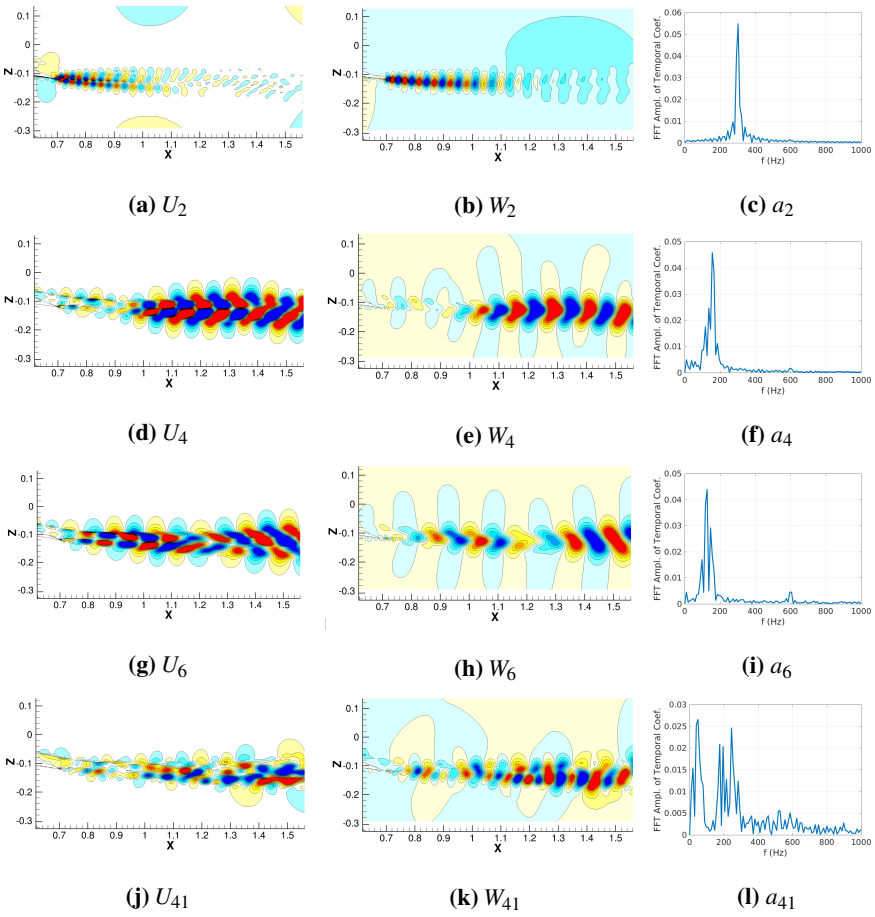

(a) U_2 **(b)** W_2 **(c)** a_2

(d) U_4 **(e)** W_4 **(f)** a_4

(g) U_6 **(h)** W_6 **(i)** a_6

(j) U_{41} **(k)** W_{41} **(l)** a_{41}

Figure 18: *Spatial modes computed with the POD corresponding to the two velocity components and FFT of the respective temporal coefficients. Indices provide the order of the mode; the first (mean) mode is omitted. Morphing case at* $300Hz$ *by means of numerical simulation.*

tions. In mode 41, a structure resembling the one of mode 27 of the non-morphed case appears attesting to the move of irregularities to lower energy ranks. As the energy of the fluctuations increases, previous modes are shifted in regions of relatively lower order. The predominant higher frequency at $350Hz$ appearing previously has vanished as it was replaced by the actuation that has moved to a higher modal rank.

Using the modal shapes and the temporal coefficients it is possible to reconstruct

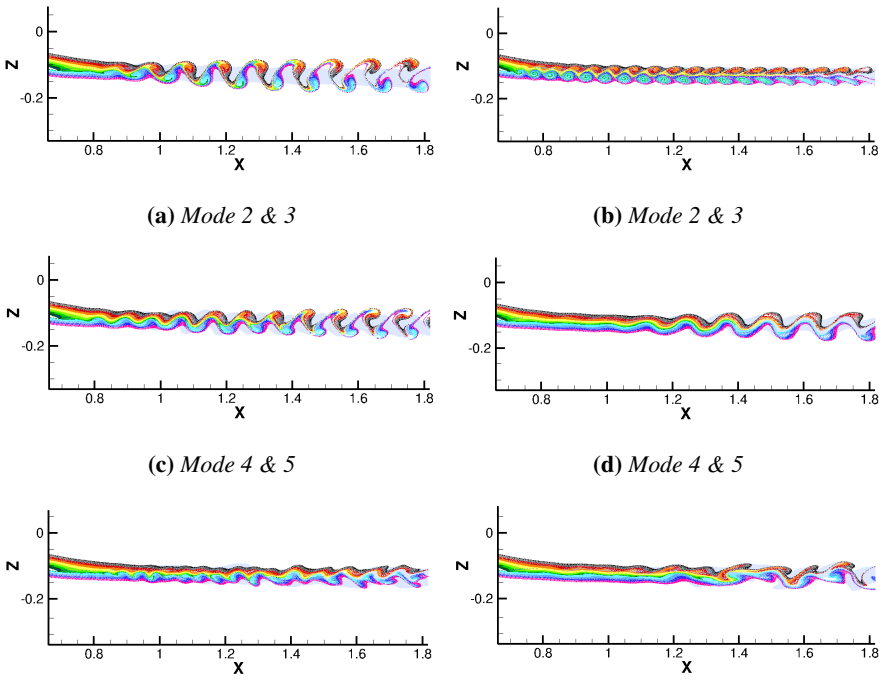

(a) *Mode 2 & 3* **(b)** *Mode 2 & 3*

(c) *Mode 4 & 5* **(d)** *Mode 4 & 5*

(e) *Higher Modes* **(f)** *Higher Modes*

Figure 19: *Development of vortical structures in the wake by means of numerical simulation, visualization with streaklines; the color of each particle represents its initial positions. Reconstruction from POD modes along with mean for STATIC (left) and* 300 *Hz (right).*

portions of the flow corresponding to different instabilities using eq. 4. This will aid in the study as it will provide a direct correspondence between the modes and the nature of the vortical structures validating previous remarks. The eddy blocking procedure can be highlighted through the change in the modal dynamics. It will also provide an overview of how flow instabilities are born and developed temporally in space. In Fig. 19 a reconstruction was carried out using each time specific modes along with the first one representing the mean flow. In Fig. 20 a cumulative reconstruction is presented where the addition of more modes results in a more accurate representation of the flow as higher order modes incorporate irregular flow phenomena.

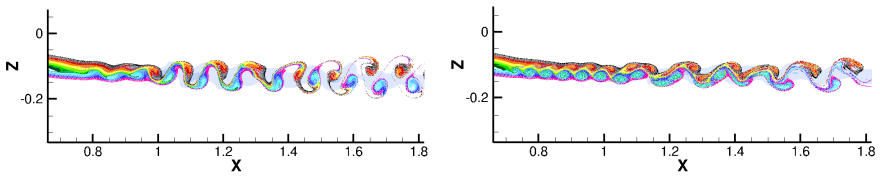

(a) *10 first modes*

(b) *10 first modes*

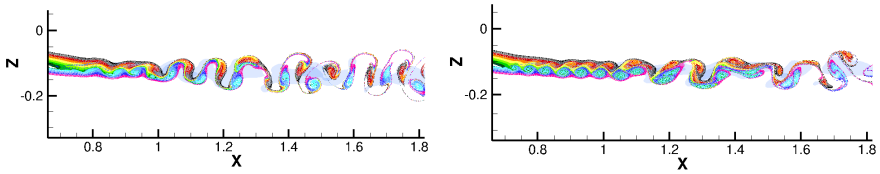

(c) *40 first modes*

(d) *40 first modes*

Figure 20: *Development of vortical structures in the wake by means of numerical simulation, visualization with streaklines; the color of each particle represents its initial positions. Reconstruction from POD modes for STATIC (left) and* 300 Hz *(right).*

In figures 19a and 19c the reconstruction of the modes provides a representation of the von Kármán and the upper shear layer instability respectively for the case where no morphing is applied. The signature of the von Kármán is prominent also close to the wing. Undulations resulting from the unstable upper layer are convected downstream and influence the alternating pattern as well. Higher order modes (above 20) presented in Fig. 19e seem to recreate the low shear layer instability. Applying the morphing with the actuation frequency of 300 Hz changes completely the first pair of modes. A low shear layer develops (Fig. 19b) and is convected downstream within a thin region. The previously existing instability tracks perfectly the actuation frequency, something that can also be evidenced in Fig. 19f from the disappearance of the low shear layer previously disposed in higher modes. The vortex pairing mechanism seems to take place after $x = 1.2m$ as it can be seen in Fig. 19d where the halving of the frequency takes place. This results to an alternating pattern that develops further away from the wing and is absolutely locked to the half of the morphing frequency. The effects of the modal changes and the mechanisms described are highlighted in the collective

reconstructions as presented in figures 20a and 20b. Figures 20c and 20d add the high order irregular phenomena in the flow to provide a comparison. The dynamics are represented quite accurately even with a reduced number of modes.

5.2.3. Mean effects on the wake

In this section a comparison on the time averaged results is carried out. In Fig. 21 the mean axial velocity profiles are plotted along the wake for various x/c non-dimensional positions. Both the z and the x axis have a zero value at the leading edge of the wing. It is evident that for frequencies lower than the natural ones of the flow (i.e. for $60Hz$ and $100Hz$) only slight changes in the profiles are visible and mostly at the early x/c stations, close to the trailing edge. For an actuation frequency close to the natural one (i.e. for $200Hz$), the wake is slightly displaced at a lower height and becomes wider. For a higher frequency ($300Hz$), a much thinner wake is visible. As the alternating shedding is suppressed until further downstream positions, the upper and lower shear layers do not spread as much, the shearing gets stronger and the velocity deficit becomes more important. For the latter morphing frequency, a smaller value of $0.15mm$ for the amplitude was also tested. The velocity profiles undergo the exact same changes and are almost indistinguishable besides some slight differences close to the minimum values. The driving parameter is the frequency and the amplitude seems to have a secondary role as long as the same order of magnitude is maintained. The results are in accordance with the analysis on the dynamic behavior carried out in the previous section. The changes in the time averaged profiles attest to the displacement of the velocity deflection points. This modifies in return the most prominent modes as seen in the previous section, something that could be validated by a stability analysis.

A complementary study of Fig. 22 attests to the same effects as some characteristic wake properties are computed. The values for the wake width, the momentum thickness, the shearing and the spreading rate of both shear layers are presented. The wake width is calculated from:

$$b_{95\%} = z^{up}_{95\%} - z^{low}_{95\%} \tag{5}$$

where $z^{*}_{95\%}$ the position for which the $u^{*}_{95\%} = 0.95 \cdot U_{inlet}$ is reached in the upper and lower shear layers respectively. The spreading rate here is defined here as the distance

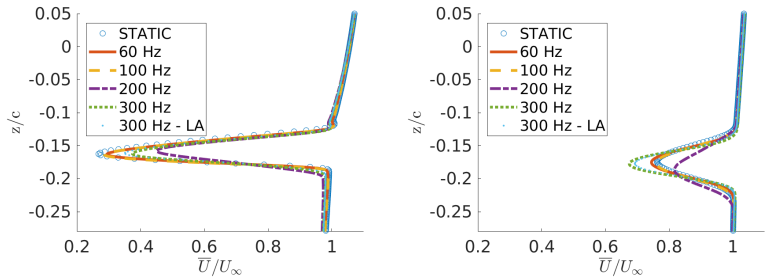

(a) $x/c = 1.1$ **(b)** $x/c = 1.4$

(c) $x/c = 1.7$ **(d)** $x/c = 2.0$

Figure 21: *Comparison of mean longitudinal velocity profiles along the wake for various actuating frequencies;numerical simulation. The amplitude is set at* 0.35*mm for every morphing application, except for the 300Hz-LA (lower amplitude) case where a value of* 0.15*mm was used.*

from the position where the halving of the inlet velocity is achieved $(z^*_{50\%})$ for each shear layer as well. The momentum thickness is computed using eq. 22c presented previously while the shearing coefficient r for each shear layer is calculated according to:

$$r_* = \frac{u^*_{95\%} - u^*_{50\%}}{z^*_{95\%} - z^*_{50\%}} \tag{6}$$

where as before, $z^*_{95\%}$ and $z^*_{50\%}$ the positions for which $u^*_{95\%} = 0.95 \cdot U_{inlet}$ and $u^*_{50\%} = 0.50 \cdot U_{inlet}$ are achieved.

In Fig. 22a the thinning of the wake is presented due to the suppression of the shedding. A linear expansion of the wake is achieved for both amplitudes tested for the $300Hz$ actuation frequency attesting to more self-similar profiles. Increasing the

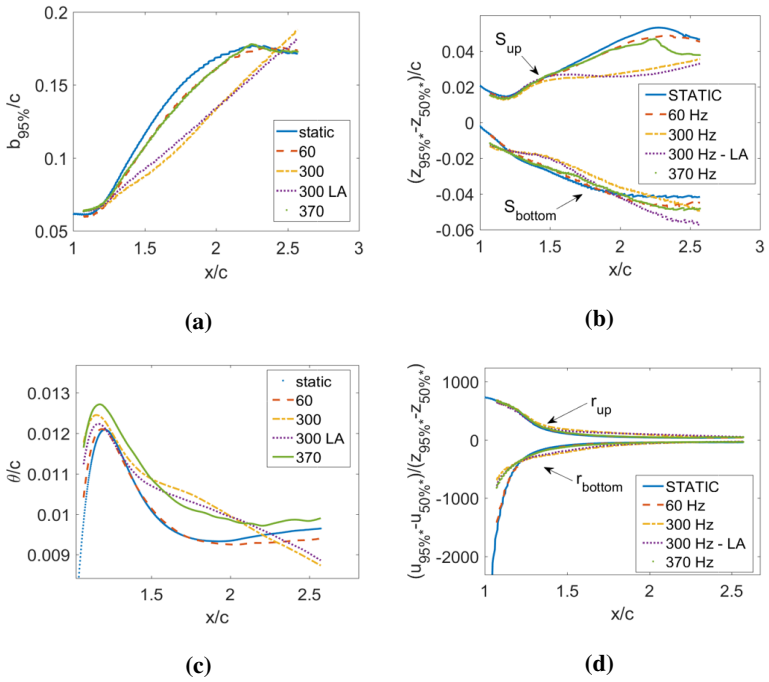

Figure 22: *Comparison of the wake characteristics for various actuating frequencies; numerical simulation. (a) Width of the wake (b) Spreading of upper (S_{up}) and lower (S_{bottom}) shear layer (c) momentum thickness and (d) shearing coefficient r; the amplitude is set at 0.35mm for every morphing application besides the 300Hz-LA (lower amplitude) where a value of 0.15 mm was used.*

frequency to even higher values (i.e. 370Hz) seems to weaken this shedding delay and the expansion returns to what has been seen for lower frequencies. This was expected from examining the dynamic response of the flow in this morphing actuation. Fig. 22b exhibits the decrease of the spreading of the upper shear layer which gets overpowered by the strengthened lower one, the interactions become weaker and finally the resulting shedding mechanism is delayed as it has been previously shown. Same as before, this mechanism does not exist for the lower frequencies tested and is weakened for the 370Hz. The r coefficient presented in Fig. 22d exhibits only slight changes while the momentum thickness is always altered as more energy is introduced in the flow.

5.2.4. Effects on the forces

The effect on the aerodynamic forces is evaluated in this section. The lift and drag coefficients are compared in Fig. 23. In Fig. 23a and 23b the effect of the actuation frequency is presented for a constant amplitude of 0.35*mm* while in Fig. 23c and 23d the effect of the amplitude is examined.

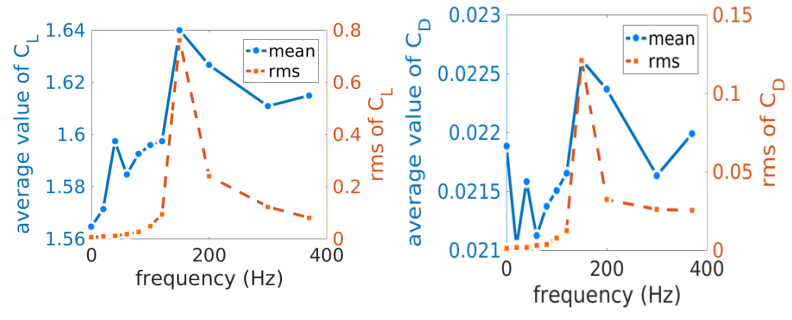

(a) *Lift coefficient*

(b) *Drag Coefficient*

(c) *Lift coefficient*

(d) *Drag Coefficient*

Figure 23: *Effect on the aerodynamic coefficients versus (top) frequency variations with a constant amplitude of* 0.35*mm and (bottom) versus amplitude for a constant frequency of* 300*Hz (left) and various frequencies (right),by means of numerical simulation; zero values for amplitude/frequency imply absence of morphing.*

Actuating in the region around the natural shedding frequency presents a prominent increase in both lift and drag mean values, accompanied with a significant increase in the fluctuations (as indicated by the root mean squared - *rms* - values) of the coefficients as well. This attests to the resonance observed in the previous section and is also in

agreement with the experimental studies included in [10]. Acting with frequencies outside this region still provides an increase in lift and in some cases a decrease in drag. The aerodynamic efficiency, expressed by the ratio of lift over drag c_L/c_D is always increased and at the same time the actuation keeps the rms levels in lower (acceptable) values. The vibration (flapping of the TE region) increases the energy attributed to the flow and produces a higher incidence effect corresponding to a lift increase. In all the morphing cases the increased aerodynamic performance could not be achieved with a static deformation of the trailing edge at the maximum displacements, attesting to the fact that the dynamic nature of the morphing application is responsible for the effects on the forces.

The amplitude variation indicates a linear response concerning the rms values which increase with the amplitude. The lift coefficient always increases while the drag coefficient initially decreases and then starts to increase again. After a specific amplitude, the value of the drag seems to be practically constant for the amplitudes examined in this article. Whether this plateau is higher or lower than the initial drag value without morphing correlates with the frequency of the actuation. Amplitude variations produce slight variations on the velocity profiles (Fig. 21). Further simulations have shown that higher amplitudes - ranging from 0.5 to 1mm - produce more significant effects. The amplitude effect on the pressure is more pronounced in all ranges, corresponding to lift and drag coefficient variations.

6. Conclusion

In this paper the electroactive morphing effects created by Macro-Fiber Composite piezoelectric patches disposed along the span of an Airbus-A320 wing have been studied by means of TRPIV and High-Fidelity numerical simulations. These actuators introduce optimal vibrations and slight deformations of the trailing-edge region. Having available a detailed experimental database and newly acquired computational results, a combined examination of high Reynolds dynamics in the wake of this supercritical wing has been carried out in respect with the aerodynamic performance increase. The main flow characteristics have been underlined. Various frequencies and some ampli-

tude combinations have been studied numerically to evaluate the morphing effects in order to enable future experiments around the same prototype, focusing on the most *optimal* morphing actuations.

The wake dynamics are significantly affected by the application of morphing when acting in frequencies close or above the natural frequencies of the separated shear layers. This has been emphasized by the POD analysis that showed new modes emerging and taking the place of naturally existing ones in positions of higher relative energy. It was assessed possible to manipulate the interactions between the different instabilities and control the generation of turbulent structures in the wake. The investigation of mean wake properties have provided a thinning of the far wake region and a suppression of the alternating pattern until later downstream regions. Thanks to the introduction of smaller-scale chaotic turbulent vortices, suppression of pre-existing predominant instability modes was achieved. Activating a shear sheltering effect an increase in the aerodynamic performance was achieved. The actuation frequency has been identified as the main driving factor for the manipulation of the dynamics in the wake.

For a constant chord section the analysis is restricted for a constant actuation frequency along the span; in the case of an actual swept wing, the variation of the chord yields a change of the local Reynolds number along the span. This should cause a shift in the local natural frequencies, even though in this Reynolds number range (order of 1 million) the modulations of the Strouhal number are moderate. Morphing in that case, can be easily adapted to be applied along the span with respect to the local modulations of the natural instability frequencies.

The aerodynamic performance gets enhanced as the mean value of the lift versus drag is found to be increased in every morphing case examined. By the present electroactive morphing concept, an order of 3.2% increase in lift has been achieved and at the same time a 1% decrease in the drag. The actuations at $60Hz$ and $300Hz$ have both achieved an increase of lift-to-drag ratio of 4%. Much alike the actuation produced by the small feathers at the edges of the wings of the large-span birds, the electroactive morphing is proven capable to achieve similar effects, inspired from the nature and targeting the design of the future wings.

Acknowledgements

The authors are grateful to the Engineering and Technical services of IMFT and LAPLACE Laboratories, to the Signal and Image Services of IMFT enabling the TR-PIV measurements, to the Software Services of IMFT enabling the MPI treatment of the TRPIV data bases on the supercomputer CALMIP, as well as to the three national supercomputing centers: CINES, IDRIS, CALMIP for having provided a significant CPU allocation for the present study. Part of this work has been carried out during the PhD fellowship granted by DGA. A special aknowledgement should be made to the SMS, "Smart morphing and Sensing for aeronautical configurations" European project (*www.smartwing.org/SMS/EU*, H2020 project N 723402) funded by the European Commission.

References

[1] S. Barbarino, O. Bilgen, R. M. Ajaj, M. I. Friswell, D. J. Inman, A Review of Morphing Aircraft, Journal of Intelligent Material Systems and Structures 22 (9) (2011) 823–877. doi:10.1177/1045389X11414084.
URL https://doi.org/10.1177/1045389X11414084

[2] A.-M. R. McGowan, A. E. Washburn, L. G. Horta, R. G. Bryant, D. E. Cox, E. J. Siochi, S. L. Padula, N. M. Holloway, Recent results from NASA's morphing project, in: Smart Structures and Materials 2002: Industrial and Commercial Applications of Smart Structures Technologies, Vol. 4698, International Society for Optics and Photonics, 2002, pp. 97–111. doi:10.1117/12.475056.
URL https://www.spiedigitallibrary.org/conference-proceedings-of-spie/4698/0000/Recent-results-from-NASAs-morphing-project/10.1117/12.475056.short

[3] X. Lachenal, S. Daynes, P. M. Weaver, Review of morphing concepts and materials for wind turbine blade applications, Wind Energy 16 (2) (2013) 283–307.

doi:10.1002/we.531.
URL https://onlinelibrary.wiley.com/doi/full/10.1002/we.531

[4] J. Scheller, M. Chinaud, J. Rouchon, E. Duhayon, S. Cazin, M. Marchal, M. Braza, Trailing-edge dynamics of a morphing NACA0012 aileron at high Reynolds number by high-speed PIV, Journal of Fluids and Structures 55 (Supplement C) (2015) 42–51. doi:10.1016/j.jfluidstructs.2014.12.012.
URL http://www.sciencedirect.com/science/article/pii/S0889974615000158

[5] G. Jodin, V. Motta, J. Scheller, E. Duhayon, C. Dll, J. F. Rouchon, M. Braza, Dynamics of a hybrid morphing wing with active open loop vibrating trailing edge by time-resolved PIV and force measures, Journal of Fluids and Structures 74 (Supplement C) (2017) 263–290. doi:10.1016/j.jfluidstructs.2017.06.015.
URL http://www.sciencedirect.com/science/article/pii/S0889974616304121

[6] B. K. S. Woods, M. I. Friswell, Preliminary Investigation of a Fishbone Active Camber Concept, American Society of Mechanical Engineers, 2012, pp. 555–563. doi:10.1115/SMASIS2012-8058.
URL https://proceedings.asmedigitalcollection.asme.org/proceeding.aspx?articleid=1720859

[7] B. K. Woods, O. Bilgen, M. I. Friswell, Wind tunnel testing of the fish bone active camber morphing concept, Journal of Intelligent Material Systems and Structures 25 (7) (2014) 772–785. doi:10.1177/1045389X14521700.
URL https://doi.org/10.1177/1045389X14521700

[8] R. F. Huang, C. L. Lin, Vortex shedding and shear-layer instability of wing at low-Reynolds numbers, AIAA Journal 33 (8) (1995) 1398–1403. doi:10.2514/3.12561.
URL https://doi.org/10.2514/3.12561

[9] S. Yarusevych, P. E. Sullivan, J. G. Kawall, On vortex shedding from an airfoil in low-Reynolds-number flows, Journal of Fluid Mechanics 632 (2009) 245–271.

doi:10.1017/S0022112009007058.
URL https://www.cambridge.org/core/journals/journal-of-fluid-mechanics/article/on-vortex-shedding-from-an-airfoil-in-low-reynolds-FBD82B2FD88CAFB463E22F35B5D4AF55

[10] M. Gharib, K. Williams-Stuber, Experiments on the forced wake of an airfoil, Journal of Fluid Mechanics 208 (1989) 225–255. doi:10.1017/S0022112089002831.
URL https://www.cambridge.org/core/journals/journal-of-fluid-mechanics/article/experiments-on-the-forced-wake-of-an-airfoil/A913D3C39F7EC63E8C41AF103DD7B7DF

[11] M. Chinaud, J.-F. Rouchon, E. Duhayon, J. Scheller, S. Cazin, M. Marchal, M. Braza, Trailing-edge dynamics and morphing of a deformable flat plate at high Reynolds number by time-resolved PIV, Journal of Fluids and Structures 47 (2014) 41–54.
URL http://dx.doi.org/10.1016/j.jfluidstructs.2014.02.007

[12] Shape-Memory Alloys Handbook.
URL https://www.wiley.com/en-us/Shape+Memory+Alloys+Handbook-p-9781848214347

[13] G. Jodin, J. Scheller, K. J. Rizzo, E. Duhayon, J.-F. Rouchon, M. Braza, Dimensionnement d'une maquette pour l'investigation du morphing lectroactif hybride en soufflerie subsonique, 2015, pp. pp. 1–13.
URL http://hdl.handle.net/2042/57219

[14] M. T. S. Tarashima, Gpu accelerated direct cross-correlation piv with window deformation, Int. Symp. on Appl. Laser Techniques to Fluid Mechanics, Lisbon, Portugal, 2010 [2] The SPMD Model: Past, Present and Future. Darema F. , In: Cotronis Y., Dongarra J. (eds) Recent Advances in Parallel Virtual Machine and Message Passing Interface. EuroPVM/MPI 2001. Lecture Notes in Computer Science, vol 2131. Springer, Berlin, Heidelberg, 2001.

[15] Y. Hoarau, D. Pena, J. B. Vos, D. Charbonier, A. Gehri, M. Braza, T. Deloze, E. Laurendeau, Recent Developments of the Navier Stokes Multi Block (NSMB) CFD solver, in: 54th AIAA Aerospace Sciences Meeting, American Institute of Aeronautics and Astronautics. doi:10.2514/6.2016-2056.
URL https://arc.aiaa.org/doi/abs/10.2514/6.2016-2056

[16] C. Hirsch, Numerical Computation of Internal and External Flows: The Fundamentals of Computational Fluid Dynamics, 2nd Edition, Butterworth-Heinemann, Amsterdam, 2007.

[17] J. Donea, S. Giuliani, J. P. Halleux, An arbitrary lagrangian-eulerian finite element method for transient dynamic fluid-structure interactions, Computer Methods in Applied Mechanics and Engineering 33 (1) (1982) 689–723. doi:10.1016/0045-7825(82)90128-1.
URL http://www.sciencedirect.com/science/article/pii/0045782582901281

[18] R. Bourguet, M. Braza, G. Harran, R. El Akoury, Anisotropic Organised Eddy Simulation for the prediction of non-equilibrium turbulent flows around bodies, Journal of Fluids and Structures 24 (8) (2008) 1240–1251. doi:10.1016/j.jfluidstructs.2008.07.004.
URL http://www.sciencedirect.com/science/article/pii/S0889974608000820

[19] D. Szubert, F. Grossi, A. Jimenez Garcia, Y. Hoarau, J. C. R. Hunt, M. Braza, Shock-vortex shear-layer interaction in the transonic flow around a supercritical airfoil at high Reynolds number in buffet conditions, Journal of Fluids and Structures 55 (2015) 276–302. doi:10.1016/j.jfluidstructs.2015.03.005.
URL http://www.sciencedirect.com/science/article/pii/S0889974615000602

[20] M. Braza, R. Perrin, Y. Hoarau, Turbulence properties in the cylinder wake at high Reynolds numbers, Journal of Fluids and Structures 22 (6) (2006) 757–771. doi:10.1016/j.jfluidstructs.2006.04.021.

URL http://www.sciencedirect.com/science/article/pii/S0889974606000429

[21] J. C. R. Hunt, I. Eames, C. B. d. Silva, J. Westerweel, Interfaces and inhomogeneous turbulence, Philosophical Transactions of the Royal Society of London A: Mathematical, Physical and Engineering Sciences 369 (1937) (2011) 811–832. doi:10.1098/rsta.2010.0325.
URL http://rsta.royalsocietypublishing.org/content/369/1937/811

[22] J. C. R. Hunt, I. Eames, J. Westerweel, Vortical Interactions with Interfacial Shear Layers, in: IUTAM Symposium on Computational Physics and New Perspectives in Turbulence, IUTAM Bookseries, Springer, Dordrecht, 2008, pp. 331–338. doi:10.1007/978-1-4020-6472-2_50.
URL https://link.springer.com/chapter/10.1007/978-1-4020-6472-2_50

[23] T. Ishihara, H. Ogasawara, J. C. R. Hunt, Analysis of conditional statistics obtained near the turbulent/non-turbulent interface of turbulent boundary layers, Journal of Fluids and Structures 53 (2015) 50–57. doi:10.1016/j.jfluidstructs.2014.10.008.
URL http://www.sciencedirect.com/science/article/pii/S0889974614002230

[24] J. Scheller, M. Chinaud, J. Rouchon, E. Duhayon, S. Cazin, M. Marchal, M. Braza, Trailing-edge dynamics of a morphing NACA0012 aileron at high Reynolds number by high-speed PIV, Journal of Fluids and Structures 55 (2015) 42–51. doi:10.1016/j.jfluidstructs.2014.12.012.
URL http://www.sciencedirect.com/science/article/pii/S0889974615000158

[25] A. Roshko, Experiments on the flow past a circular cylinder at very high Reynolds number, Journal of Fluid Mechanics 10 (3) (1961) 345–356. doi:10.1017/S0022112061000950.

URL https://www.cambridge.org/core/journals/journal-of-fluid-mechanics/article/experiments-on-the-flow-past-a-circular-cylinder-at-7859A6C46BF4B0F43F11F52AE1C60150

[26] Y. Hoarau, D. Faghani, M. Braza, R. Perrin, D. Anne-Archard, D. Ruiz, Direct Numerical Simulation of the Three-Dimensional Transition to Turbulence in the Incompressible Flow around a Wing, Flow, Turbulence and Combustion 71 (1) (2003) 119–132. doi:10.1023/B:APPL.0000014931.01400.7e.
URL https://doi.org/10.1023/B:APPL.0000014931.01400.7e

[27] M. Braza, D. Faghani, H. Persillon, Successive stages and the role of natural vortex dislocations in three-dimensional wake transition, Journal of Fluid Mechanics 439 (2001) 1–41. doi:10.1017/S002211200100458X.
URL https://www.cambridge.org/core/journals/journal-of-fluid-mechanics/article/successive-stages-and-the-role-of-natural-vortex-dis-B704A7018B90449A8A548327B731A88B

[28] G. Berkooz, P. Holmes, a. J. L. Lumley, The Proper Orthogonal Decomposition in the Analysis of Turbulent Flows, Annual Review of Fluid Mechanics 25 (1) (1993) 539–575. doi:10.1146/annurev.fl.25.010193.002543.
URL https://doi.org/10.1146/annurev.fl.25.010193.002543